Kondo-Ising and tight-binding models for TmB_4

John Shin, Zack Schlesinger, and B. Sriram Shastry
Physics Department, University of California, Santa Cruz, California 95064, USA
(Received 24 February 2017; revised manuscript received 27 April 2017; published 26 May 2017)

In TmB_4, localized electrons with a large magnetic moment interact with metallic electrons in boron-derived bands. We examine the nature of TmB_4 using full-relativistic *ab initio* density functional theory calculations, approximate tight-binding Hamiltonian results, and the development of an effective Kondo-Ising model for this system. Features of the Fermi surface relating to the anisotropic conduction of charge are discussed. The observed magnetic moment $\sim 6\ \mu_B$ is argued to require a subtle crystal field effect in metallic systems, involving a flipped sign of the effective charges surrounding a Tm ion. The role of on-site quantum dynamics in the resulting Kondo-Ising type "impurity" model are highlighted. From this model, elimination of the conduction electrons will lead to spin-spin (RKKY-type) interaction of Ising character required to understand the observed fractional magnetization plateaus in TmB_4.

DOI: 10.1103/PhysRevB.95.205140

I. INTRODUCTION

TmB_4 is a metallic frustrated magnet, with an Ising-like antiferromagnetic ground state [1]. Experiments have shown a variety of rich phenomena—along with the fractional magnetization plateaus at low temperature (occurring at fractions of the saturation magnetization, with a stable plateau at 1/2, and fractional plateaus at 1/7, 1/8, 1/9,... [1]) and its rich phase diagram, hysteretic magnetoresistance and the anomalous Hall effect have also been observed [2]. Fractional magnetization plateaus for 2D quantum spin systems were first observed in $SrCu_2(BO_3)_2$ [3] and later observed in the family of rare-earth tetraborides [1], where the rare-earth ions can be mapped onto the Shastry-Sutherland lattice [4] and the boron atoms can be grouped into B_6 octahedra and dimer pairs [5,6]. In contrast to the high fields necessary to reach magnetic saturation in $SrCu_2(BO_3)_2$ [3], TmB_4 saturates at fields on the order of 4 T [7] and also exhibits long-range order [8]. This magnetic analog to the fractional quantum Hall effect and relatively simple example of geometric frustration has spurred both theoretical and experimental interest, where the juxtaposition of 2D magnetism and 3D conduction [2,9] remains novel.

The primary focus of this paper is on the electronic and magnetic characteristics of TmB_4, however, TmB_4 also has interesting structural aspects and it is worthwhile to take a moment to review them. The thulium atoms lie in sheets oriented perpendicular to the tetragonal c axis. Their structure can be viewed in terms of tiling of squares and triangles in a classical manner examined by Archimedes. Between these Tm sheets there are planes of boron atoms. Boron, adjacent to carbon in the periodic table, might be expected to form 6-element rings, as indeed it does in TmB_2 [10], however, in TmB_4 boron atoms form *7-atom rings* that lie in planes consisting of the 7-atom rings and squares.

The Tm is nominally trivalent and has a $4f^{12}$ configuration. This leads to a two-hole state on the Tm with a local moment of $M_J = \pm 6$. This local moment interacts and hybridizes with conduction electrons associated with boron bands. This paper seeks to capture the essence of that interaction and hybridization. It includes an *ab initio* approach, tight-binding model calculations associated with reduced structures, and, most notably, the development of an effective Kondo Ising model for which an understanding of the symmetry of the Tm site is critical.

II. STRUCTURE

TmB_4 crystallizes in a tetragonal structure (space group $P4/mbm$) [11] and has a mixture of 2D and 3D aspects. The Tm lattice viewed on its own consists of stacked 2D sheets, with each sheet a 2D Shastry-Sutherland lattice [4]. Each sheet has a structure that includes perfect squares and nearly equilateral triangles of Tm atoms, as shown in Fig. 1(a). Each Tm ion has five near Tm neighbors in the plane with angles between near neighbor bonds of 90, 59, 59, 90, and 62 degrees, where 90 is the interior angle of a square and 59 and 62 are the interior angles of an almost equilateral triangle. These Tm sheets lie in the crystalline a-b plane and are stacked along the c axis. The distance between Tm sheets is .399 nm.

Boron planes lie halfway between the Tm sheets. The structure of a boron plane involves a mixture of 7 atom rings and 4 atom squares as shown in Fig. 1(b). There are two distinct types of boron sites in these planes. One type, shown in blue, is solely part of the boron plane. The other type, shown in light gray, is part of the boron plane and also of an octahedral chain along the c axis. This second type comes in groups of 4 atoms which form a square in the plane [Fig. 1(b)] and are part of an octahedron which includes apical boron atoms which are not in the plane and are thus not shown in Fig. 1(b).

On the other hand, the pure planar boron atoms (blue) come in dimer pairs as shown in Fig. 1(b). There are no extra-planar boron above or below them, thus their $2p_z$ orbitals are unencumbered. It is the partially occupied $2p_z$ orbital of these pure planar boron atoms that couple most strongly to Tm $4f$ level electrons. Most of the essential nature of the hybridization of TmB_4 can be captured by studying the structures shown in Fig. 1(b) and Fig. 1(c). In a later section we discuss tight-binding results for these structures and compare those to our DFT results. One of our primary goals is to see how far one can go along the path of structural simplification while still capturing the essential nature of the interaction between the quasilocalized f state and itinerant $2p$ states and thus the magnetic character and essential phenomenology of TmB_4.

 ©2017 American Physical Society

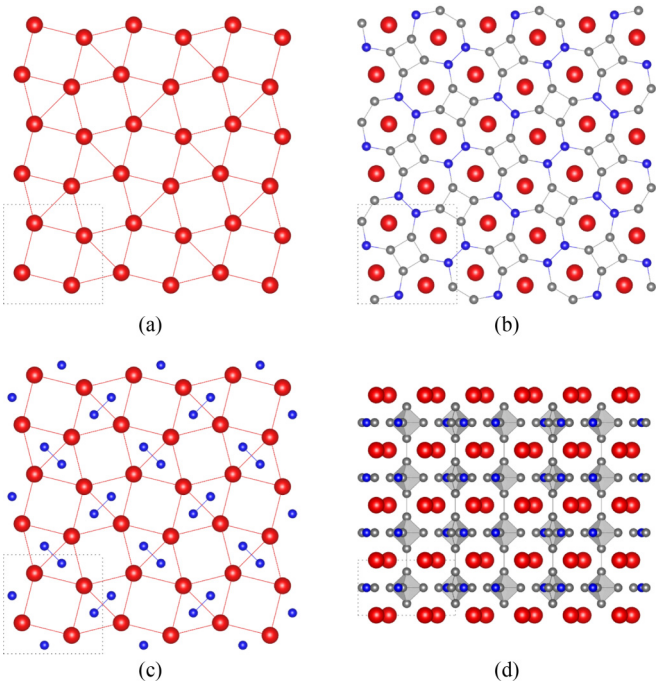

FIG. 1. (a) Figure 1(a) shows the structure of a single plane of Tm atoms within crystalline TmB_4. Note the triangle and square tiling. (b) Figure 1(b) shows the juxtaposition of a plane of Tm atoms (red) and a plane of B (blue and gray) atoms as viewed from above. The Tm plane is .20 nm above the boron atoms plane. Coupling of the Tm f orbital to the planar boron $2p_z$ band plays an essential role in the physics and phenomenology of the system. Note the 7 atom boron rings. (c) In Fig. 1(c) only the dimer boron atoms and the Tm atoms are shown. This figure shows the most simplified structure able to capture the essence of the magnetism and coupling in TmB_4. (d) Figure 1(d) shows the structure of TmB_4 as viewed from the side (along the a axis). One sees the stacking of the Tm layers in red, the blue and gray boron planes, and in addition the chain formed by boron octahedra oriented along the c axis. The apical boron are colored gray.

Figure 1(d) shows the full 3D structure of TmB_4. This includes the alternating boron and Tm planes, as well as apical boron atoms (gray) which lie between the boron and Tm planes. These are located above and below squares of B atoms in the plane and form the tops and bottoms of the boron octahedra which stack along the c axis creating chains which extend throughout the crystal. These chains of boron octahedra are shown to not couple strongly to the Tm orbitals and thus do not play a large role in the magnetic character of TmB_4.

The local environment of Tm can be described by a model as shown in Fig. 2. Above and below the Tm are 7 atom boron rings, three of which are the previously mentioned dimer borons. Apical boron lie above and below the boron planes. There are mirror plane symmetries through the Tm plane and perpendicular to the dimer-dimer bond, and a total of 18 borons construct the local environment.

III. DENSITY FUNCTIONAL THEORY CALCULATIONS

To begin our exploration of the electronic and magnetic characteristics of TmB_4, we have performed spin-polarized full relativistic density functional theory [12] calculations [13] with the full potential local orbital (FPLO) code (version 14.00-48) [14], using the generalized gradient approximation (GGA), along with an intra-atomic Hubbard U repulsion term. The PBE96 [15] and atomic limit functionals [16,17] were used for the GGA and U, respectively, with a k mesh of 24^3 in the Brillouin zone. Values of $U = 8$ eV and $J = 1$ eV were used on the Tm $4f$ orbitals. The lattice constants and atomic positions were taken from experiment [11]. An LDA+U study of rare-earth tetraborides has previously been undertaken in Ref. [5], but here we focus on the case of TmB_4. We note that there are limitations of the LDA+U method in fully describing highly correlated systems [18], which is exemplified by a reduced magnetic Tm moment of $M_J = 3.38$ found in our metastable ground state compared to experiment [1], but the method has been used with success in other lanthanide systems [10,19–21].

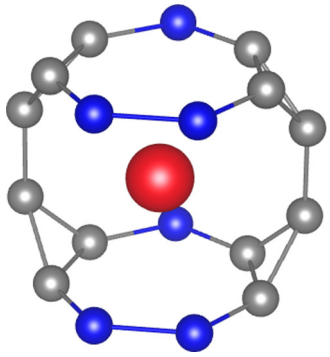

FIG. 2. This shows Tm (red) and its local environment. The blue spheres indicate the dimer boron, while the gray spheres indicate the boron that participate in the formation of octahedra.

Many initial occupation matrix configurations [22] were investigated, but the results shown here depict the convergence of a calculation with two initial holes starting in the high moment $|7/2, \pm 7/2\rangle$ and $|7/2, \pm 5/2\rangle$ states, with induced ferromagnetic order to supply a nonzero moment. Since the Hund's rules ground state [5] and antiferromagnetic order can break the crystal space group symmetry, we have also investigated reductions in symmetry with both ferromagnetic and antiferromagnetic order, but none converged to a metastable solution. For the correlated $4f$ orbitals, we find a configuration of $4f12.03$ and thus an inference of about 1.97 holes per Tm in high-spin f states.

The band structure obtained using the DFT+U calculation is shown in Figs. 3(a) and 3(b) where the vertical axis represents the energy of the Kohn-Sham eigenstate and the horizontal axis shows the position in the first Brillouin zone. In Fig. 3(a), we focus on dispersion in the a-b plane, where $\Gamma = (0,0,0)$, $X = (0, \frac{\pi}{b}, 0)$, $M = (\frac{\pi}{a}, \frac{\pi}{b}, 0)$, and a, b, and c are the lattice constants (where $a = b$ in this case). The bands exhibit "band-sticking" [23] at high symmetry points due to the nature of the nonsymmorphic space group, which contains a screw axis.

These plots show the rapidly dispersing bands associated with boron $2p$ orbitals along with rather flat bands associated with Tm $4f$ orbitals. We have circled two bands which show significant $4f$-$2p_z$ planar hybridization at the M point.

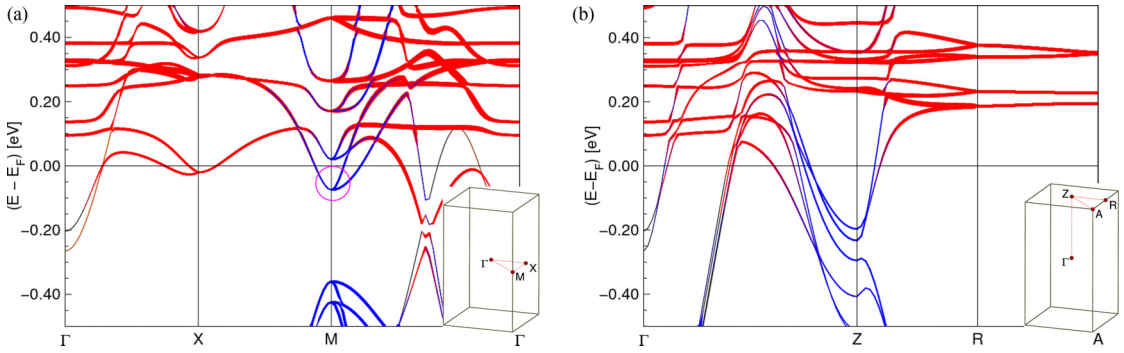

FIG. 3. (a) Band structure for TmB_4 from the DFT calculation, which shows dispersion in the a-b plane. The inset shows the path taken in the BZ, Γ-X-M-Γ. Red indicates Tm $|J = 7/2\rangle$ weights, while blue indicates dimer B $|J = 3/2, m_J = \pm 1/2\rangle$ weights. We have circled a region that shows strong $4f$-$2p_z$ hybridization, which occurs at the M point, with a magenta circle. There are electron pockets around Γ, X, M, and along the M-Γ path. (b) Dispersion along the c axis, where the inset shows the path taken in the BZ, Γ-Z-R-A. There are electron pockets around the Z point and hole pockets along the Γ-Z path. $4f$-$2p_z$ hybridization can be seen along the Γ-Z path and around the Z point. There is some $5d$-$2p_z$ hybridization around the Z point (not shown).

The M point is of particular interest due to significant hybridization between the $4f$ and $2p_z$ orbital that occurs there. At the M point two boron dimer bands dip just below the Fermi level and there is a pocket of occupied states which are of $4f$-$2p_z$ hybrid character. The M point represents propagation along the in-plane diagonal in real space. It includes the four propagation directions which are parallel to the bonds between dimer boron atom pairs.

In Fig. 3(b) we show c-axis dispersion, where the path taken in the BZ is Γ-Z-R-A, where $Z = (0,0,\frac{\pi}{c})$, $R = (0,\frac{\pi}{b},\frac{\pi}{c})$, and $A = (\frac{\pi}{a},\frac{\pi}{b},\frac{\pi}{c})$. There is $4f$-$2p_z$ hybridization along the Γ-Z path and around the Z point. In addition, there is also some $5d$-$2p_z$ hybridization around the Z point (not shown). We have four hole pockets along Γ-Z and two electron pockets around the Z point.

In Fig. 4(a), we show the full Fermi surface, where the large surface along Γ-Z is a hole surface and the rest are electron surfaces. The Fermi surfaces shown in previous measurements of the related rare-earth tetraboride YB_4 [24] can be clearly identified along the Γ-Z direction. We can see examples of the aforementioned surface nesting around M and Z. We have also taken x-y cross sections at the Γ point and at $2Z/5$, to show how the surfaces nest. We can see that the cross section at $2Z/5$ shows four hole surfaces, which can be grouped into two pairs, a larger pair and smaller pair. They exhibit quasi-1D behavior, as indicated by the relatively flat portions of the surfaces. For these surfaces, from largest to smallest, we have calculated the ratio of the effective masses at the $2Z/5$ point to be $\|m_{zz}/m_{xx}\| = 0.081, 0.076, 0.15$, and 0.093. We have also calculated the dHvA frequencies for the extremal cross-sectional areas in the plane defined by the k_z axis for four major surfaces in Table I: the largest of the quasi-1D surfaces along the Γ-Z path [the large magenta surface in 4(a), and the largest in the $2Z/5$ cross section], the larger M point surface [the surface in the midpoint of the edge of the side faces in 4(a), whose pair can be seen in 4(b)], the larger Z point surface [the surface at the top and bottom faces found in 4(a), whose pair can be seen in 4(c)], and the large surface around the Γ point, of which we can see the cross-sectional area in 4(a).

In Figs. 4(b) and 4(c), we show the Fermi surface for a single hybridized $4f$-$2p_z$ band centered at the (b) M point and the (c) Z point to show the anisotropy of the hybridization. There is a "dumbbell" shaped surface centered at the M point and a "football" shaped surface centered at the Z point.

IV. TIGHT-BINDING MODELS

A goal of our tight-binding calculations is to reproduce essential features of the bands using simplified models. We will focus purely on planar dispersion. Our first simplification is to ignore the apical boron atoms and to perform a tight-binding calculation involving coupled planes of B and Tm atoms. This calculation will show very little c-axis dispersion, however, it will capture essential features of the ab plane dispersion and the coupling between Tm f orbitals and boron $2p$ bands. We include a single Tm $4f$ orbital which couples to boron $2p_z$ orbitals via the parameter V. In this calculation we use a single $2p_z$ orbital for the boron atoms, as the other $n = 2$ orbitals of the planar boron are involved in bonding [5,6,25], which are localized and noninteractive. This is what one expects based on the observed structure and threefold planar bonding, and it is confirmed by our DFT calculation, where the dimer boron $2p_z$ orbital hybridizes with the $4f$ level. The unit cell of this simplified model is shown in the inset to Fig. 5, where there

TABLE I. dHvA frequencies for four major surfaces. The frequencies are in 10^3 Tesla. The extremal cross-sectional areas are shown for planes defined by the k_z axis. The four surfaces can be seen in Fig. 4(a), where the Γ-Z surface is the large magenta surface, the larger M point surface is found on the midpoint of the edge of the side faces, the Z point surface is found on the top and bottom faces, and the Γ point surface is shown in the bottom cross section, which touches the BZ boundaries. Only the M point surface has a nonvanishing cross-sectional minimum.

	Γ-Z	M	Z	Γ
Max F (kT)	0.75	0.44	0.058	1.40
Min F (kT)		0.051		

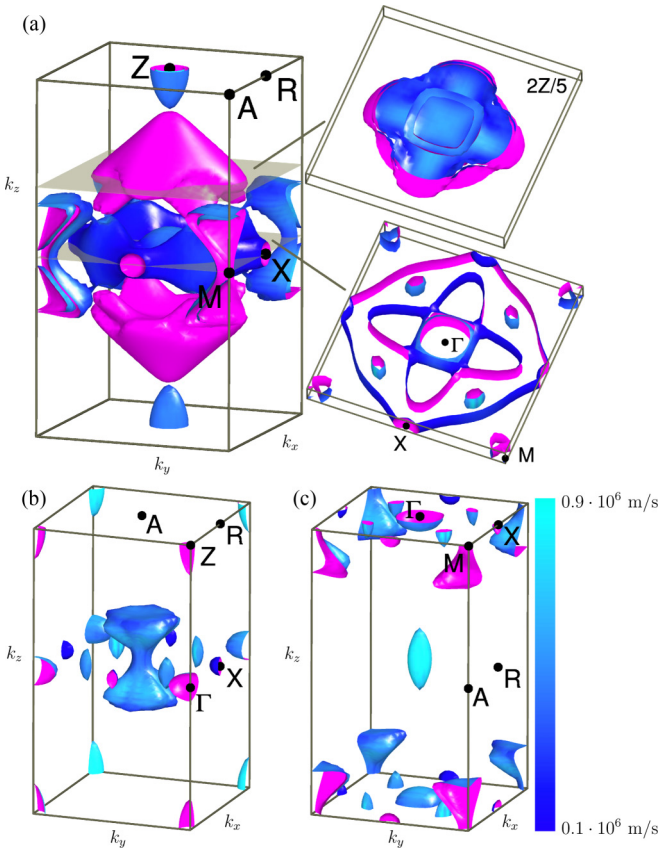

FIG. 4. Fermi surface from the DFT calculation, where the color indicates the magnitude of the Fermi velocity, as indicated by the color map. In (a), we show the full Fermi surface, centered at the Γ point. Surfaces with an exterior blue gradient represent electronlike surfaces, while surfaces with magenta exteriors are holelike surfaces: Thus, the large (magenta) surface along the Γ-Z path is a quasi one-dimensional hole surface since it is flatter in the x-y directions compared to z, while the others are electron surfaces. We have taken x-y cross sections of the electronlike surface at the Γ point and of the holelike surface at $2Z/5$, where the cross sections have been given some height in the z direction to show the curvature. In (b) and (c), we focus on a single hybridized $4f$-$2p_z$ band, centered at (b) the M point and (c) the Z point to better showcase the symmetry of the hybridized surfaces. The electron surface centered in (c) shows quasi-2D conduction, with a planar effective mass ratio of $|\frac{m_{xx}}{m_{zz}}| = 0.067$ near the tip of the surface. For the quasi-1D surface, we estimate an m_{zz} of $0.46\,m_e$ near $2Z/5$, while for the quasi-2D surface, we estimate an m_{xx} of $0.29\,m_e$ near the tip. We also estimate carrier concentrations of 0.05, 0.04, 0.01, and 0.006 per cell for the four hole surfaces, and 0.006 and 0.004 per cell for the Z point surfaces. The volume of the unit cell is $1.98 \cdot 10^{-28}$ m^3.

are 4 Tm sites, eight equatorial or side sites (gray), and four dimer sites (blue).

We use the parameter t to quantify the B to B hopping and V for the coupling between the B $2p_z$ orbital and the Tm f level. A small hopping parameter for in-plane Tm to Tm hopping T is also employed to give the Tm bands a little width. In Eq. (1) and Eq. (2), $|\phi\rangle$ represents the planar boron $2p$ wave function, while $|\psi\rangle$ represents the Tm $4f$ wave function. In the first term, we have hopping between the boron and its

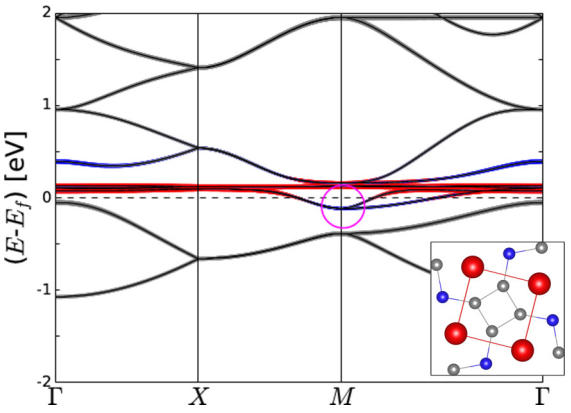

FIG. 5. Band structure of a simplified tight-binding model, where the apical boron has been removed. Tight-binding band dispersion is calculated for $t = -1.0$ eV, $V = -0.04$ eV, and $T = -0.01$ eV with site energies of 1.95 eV for the planar B and 0.1 eV for the Tm f orbital. Red lines reflect contributions from the Tm f eigenvector, while blue and gray indicate dimer and octahedral boron, respectively. The analog of the two hybrid bands from the DFT calculation can be seen below the Fermi level ($E_F = 0$) at the M point, circled in magenta. The inset shows the unit cell for this simplified model.

three nearest neighbors. Next, we have coupling between the Tm wave function and its seven boron nearest neighbors, and finally, we have hopping between the Tm and its five near neighbors.

$$\hat{H}_{TB} = t \sum_{<i,j>} |\phi_i\rangle \langle\phi_j| + V \sum_{<i,j>} |\psi_i\rangle \langle\phi_j| + T \sum_{<i,j>} |\psi_i\rangle \langle\psi_j| + \text{H.c.} \quad (1)$$

In Fig. 5 we show results for the band structure for this tight-binding model. Γ is the center of the first BZ, i.e., the point at which $\vec{k} = \vec{0}$; X is the side of the face and M is the corner. All of these represent in-plane dispersion. The M point is of particular interest as considerable coupling between $4f$ and $2p_z$ states occurs there. This tight-binding calculation reproduces the pocket of occupied states of mixed $4f$ and $2p$ character in this region, where the analog of the two hybrid bands highlighted in Fig. 3(a) can be seen just below the Fermi level ($E_F = 0$), where the bands are degenerate from X-M and split from M-Γ.

Tight-binding results from an even more simplified structure are shown in Fig. 6. Because the Tm couples most strongly to the dimer boron, as inferred from our DFT results, we have also created a tight-binding model with just the Tm and dimer boron atoms, as illustrated in Fig. 1(c) and in the inset to Fig. 6, where the unit cell contains four Tm sites and four dimer sites. This calculation shows the two bands of mixed f-p character at the M point near the Fermi level ($E_F = 0$) as in the previous TB calculation and in the DFT calculation. We have incorporated an additional parameter t_2 which connects the pairs of borons. In Eq. (2), we have nearest neighbor hopping between the pairs of dimers, coupling between the Tm and its three dimer nearest neighbors, hopping between Tm sites, and a next nearest neighbor hopping which connects the isolated

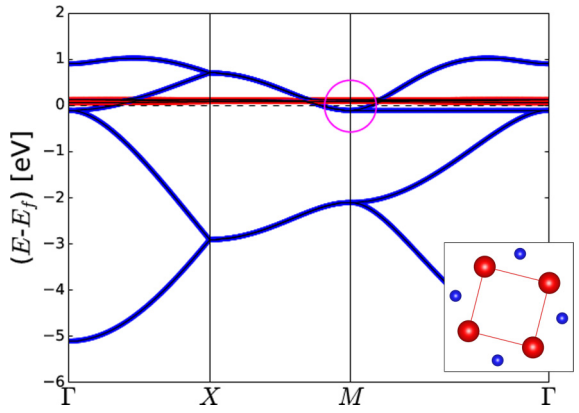

FIG. 6. Band structure of the further simplified tight-binding model, where the octahedral boron have been removed. Tight-binding band dispersion is calculated for $t = -1.0$ eV, $V = -0.04$ eV, $t_2 = -0.75$ eV, and $T = -0.01$ eV with site energies of -1.1 eV for the planar B and 0.1 eV for the Tm f orbital. The analog of the two hybrid bands from the DFT calculation can be seen mixing at the M point near the Fermi level ($E_F = 0$), circled in magenta. The inset shows the unit cell for this further simplified model.

dimers, which is necessary for dispersion in this model. In these models, one could duplicate the pocket at the X point found in the DFT band structure as in Fig. 3(a) with a complex hopping parameter on the Tm lattice, but we have omitted this for simplicity.

$$\hat{H}_{TB} = t \sum_{<i,j>} |\phi_i\rangle \langle\phi_j| + V \sum_{<i,j>} |\psi_i\rangle \langle\phi_j| + T \sum_{<i,j>} |\psi_i\rangle \langle\psi_j| + t_2 \sum_{\ll i,j\gg} |\phi_i\rangle \langle\phi_j| + \text{H.c.} \quad (2)$$

V. SIMPLIFIED CRYSTAL FIELD PHYSICS OF THE Tm ION IN TmB_4

In order to build up our understanding of the Kondo type model, and further a suitable interacting model of the spins, we need to make several approximations. We will simplify matters from the formally exact but technically formidable periodic Anderson lattice model and view the Tm initially as an impurity embedded in the B lattice. In a unit cell one has four inequivalent Tm ions, but each has the same local environment that is rotated relative to the others. We consider any one Tm as our impurity and describe its CF level structure next. The Tm^{3+} ionic state has a f^{12} configuration, leading to an even number of electrons. It thereby evades the Kramers degeneracy that is responsible for Ising like behavior in many clean examples, such as the case of Dy^{3+} ions in $DyBa_2Cu_3O_{7-\delta}$ [26,27], which is an excellent realization of the famous 2-d Ising model of Onsager [28]. Therefore the origin of the Ising like behavior reported in experiments with $m \sim \pm 6$ requires some explanation. Towards this end we present a simple crystal field (CF) theory calculation using a point charge crystal field model [29]. The results of this model need to be taken with caution in a metallic system, since the charges are smeared in a metallic system, as opposed to an insulator.

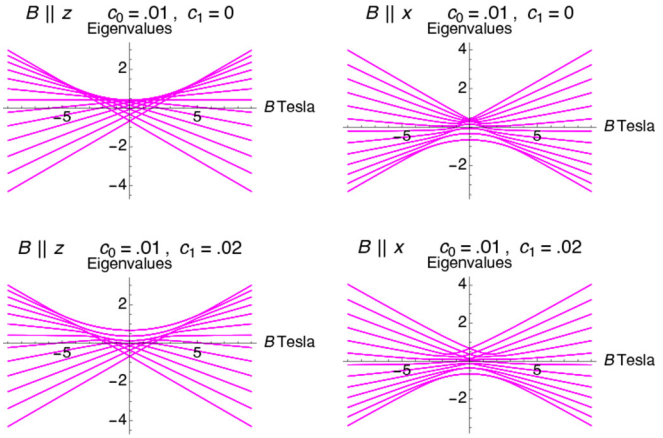

FIG. 7. The full spectrum of H_{CFZ} the crystal field plus Zeeman Hamiltonian with magnetic field along z axis (panels at left), or along x axis (panels at right) from Eq. (8) with $c_0 = .01$ meV, and $c_1 = 0$ meV (top left and top right) or $c_1 = 0.02$ meV (bottom left and bottom right). The top-left panel illustrates the effective Ising nature of the Tm moment in the z direction with a linear evolution of the lowest energy with field $B||z$ over a wide range. We see here the necessity for choosing $c_0 > 0$; inverting its sign also inverts the spectrum and the ground state then would be non-Ising-like for fields $B_Z \lesssim 5$ Tesla. The top-right panel shows that a field along the x axis $B||x$, the lowest level is not linear, but for fields around 6 T the linearity is recovered with a slope (i.e., the magnetic moment) $\sim 6\ \mu_B$. The two lower panels have a nonzero value of the transverse terms, i.e., $c_1 \sim 0.02$ meV. This does not create a noticeable gap in the level crossing at zero field in the z direction, while a larger value would do so. It thus appears that we can ignore c_1 for many (but not all) purposes, as explained in the text.

We make one important change from standard CF theory; the sign of the crystal field energy is taken to be opposite of the usual one valid in an insulator. An f electron on Tm^{3+} will be taken to experience an attractive (rather than repulsive) force from the B sites. The repulsive interaction sign convention inverts the spectrum and gives a vanishing moment, clearly a wrong result. This can be seen from the spectrum of the ionic Hamiltonian in Fig. 7, where the opposite sign simply inverts the spectrum.

Flipping the sign of the CF interaction in metallic systems has a well established precedent. In the case of rare earths (including Tm) in noble metal (Au and Ag) hosts, the significant work of Williams and Hirst in Ref. [30] shows that the observed moment requires such a flipped sign. Flipping the sign in Ref. [30] (see also Ref. [31] pages 171–173) was ascribed to the presence of 5d electrons in the rare earth, which are argued to form a virtual bound state at the Fermi level. The polarizable nature of this virtual bound state is taken to allow for such a flipping. The DFT calculation shows an occupied 5d state, along with many negative hopping integrals for the corresponding Tm and B Wannier functions, which would support this argument.

An independent argument made below invokes the weakly electronegative nature of the boron atom. It is not completely clear as to which of the two rather qualitative arguments is ultimately responsible for the final effect, but since the latter is simple enough, we present it anyway. We will choose the

point charges at the boron atoms to be *positive*, corresponding to an ionized state lacking some electrons. This change is motivated by the knowledge that in the metallic state being modeled, the boron atom donates its electrons towards band formation. It is thus very far from the ionic limit in an insulator, where the atom might be imagined to have captured some electrons. This contrasting situation is realized by the fluorine atom in $LiHoF_4$ or the oxygen atom in stoichiometric high T_c parent compound La_2CuO_4. The relevant atoms F and O have a high electron affinity, and therefore grab one and two electrons, respectively, in the solid, and may thus be visualized as negatively charged. Thus we might expect that the boron atom, with its considerably smaller electron affinity Ref. [32], plays a role closer to that of an anion, rather than a cation, in order to reconcile the data on TmB_4.

For this purpose we consider the total electrostatic potential at the location of a Tm ion, produced by its neighborhood of 18 boron atoms located as follows: the four apical sites, [33], the six dimer sites [34], where two of the borons are a larger distance away from the Tm site, and the eight "side" boron which form the equator of octahedra [35]. We can visualize these sites as in Fig. 2. Assuming an attractive Coulomb interaction between the electron and each boron atom, the Coulomb energy can be expanded at the Tm site, assumed to be the origin, and leads to

$$V_{CF} = V_0 + V_1(x+y) + V_2(x^2+y^2-2z^2-\alpha\, xy) + O(r_\alpha^3), \tag{3}$$

where V_0, V_1, and $V_2 = 0.0432942$ are constants, $\alpha = 5.39965$ and the neglected terms are of third and higher order in the components of the vector $\vec{r} = \{x,y,z\}$ locating the Tm ion. If we choose a repulsive interaction, as appropriate for the case of say $LiHoF_4$ or stoichiometric La_2CuO_4, the Coulomb interaction would be chosen as repulsive. Thus flipping the sign of our final result would give the repulsive case.

Observe that this series contains odd terms in the coordinates; this is due to the lack of inversion symmetry about the Tm ion. One implication is that we expect to see optical transitions between different crystal field levels. It would be interesting to pursue this using optical methods, especially since Tm^{3+} ions are studied in infrared laser materials [36,37]. From Eq. (3) we can construct an effective local spin Hamiltonian by using the Wigner Eckhart theorem (W-E). This procedure can be automated for ions having a simple symmetry, as in the Stevens effective Hamiltonian theory [29]. In the present case the symmetry of Tm site is very low and hence it is more useful to build up our understanding from the basics. The manifold of angular momentum $|J| = 6$ states, arising from the Hunds rule as $\vec{J} = \vec{L} + \vec{S}$, with $|L| = 5$ and $|S| = 1$, is the basis for the representation of all vector operators. The W-E theorem helps us to replace the components of the vector x,y,z by operators proportional to J_x, J_y, J_z. More generally we set

$$r_\alpha^n \to M_n J_\alpha^n, \tag{4}$$

where M_n is the W-E reduced matrix element. Due to parity of the $4f$ matrix element, only terms in r_α^n with even n survive [38]. Therefore to second order, we write the effective local Hamiltonian as

$$H_{CF}/c_0 = (J_x^2 + J_y^2 - 2J_z^2) - \frac{\alpha}{2}(J_x J_y + J_y J_x) \tag{5}$$

$$= J(J+1) - 3J_z^2 + i\frac{\alpha}{4}\left(J_+^2 - J_-^2\right), \tag{6}$$

where we used a symmetrization rule for noncommuting operators to express the xy term in Eq. (3) in terms of components of J in Eq. (5). Here c_0 $(= V_2 M_2^2)$ is a constant that lumps together the reduced matrix element, shielding factors, and other details—it is usually best to determine it from experiments. This theory is missing the fourth and higher order terms in r_α; these need not be small but one expects that the low order theory given by Eq. (6) provides the correct starting point for discussing the CF splitting of the $J = 6$ level.

In Eq. (6) we see that if $\alpha = 0$, the leading term in the Hamiltonian has an exact Ising like symmetry leading to a degenerate minimum at $J_z = \pm 6$. However since α is estimated above to be nonzero, this symmetry cannot be exact, and we must examine the solution further. If we use the raising and lowering terms with coefficient α as a perturbation of the leading term, the degeneracy is lifted to the sixth order, and the resulting states will be two distinct linear combinations of the maximum $|m| = 6$ states, with amplitudes for lower $|m|$. We can also calculate the eigenstates numerically; a simple calculation yields the two low lying solutions

$$\begin{aligned} E_a/c_0 &= -78.5199, \\ \Psi_a &= \{-0.559111, 0, -0.319154\,i, 0, 0.245299, 0, \\ &\quad 0.225227\,i, 0, -0.245299, 0, \\ &\quad -0.319154\,i, 0, 0.559111\} \\ E_b/c_0 &= -75.4681, \\ \Psi_b &= \{-0.640364, 0, -0.276433\,i, 0, 0.116273, 0, 0, \\ &\quad 0, 0.116273, 0, 0.276433\,i, 0, -0.640364\}, \end{aligned} \tag{7}$$

where the wave functions are expressed in the basis $|m\rangle$, $m = 6,5,\ldots -5,-6$. As expected from the perturbative argument, the two states are distinct linear combination of $|m\rangle$ states with $m = 6,4,2,0,-2,-4,-6$, the skipping of odd m is as required by the form of the perturbation term $i\frac{\alpha}{4}(J_+^2 - J_-^2)$. The signs of the coefficients imply that the two states are derived from the sum and difference of the two degenerate states $m = \pm 6$. Each state also has a vanishing expectation of J_z and is orthogonal to each other. Thus, in the absence of a magnetic field, the two lowest states, split off from higher energy states by a gap, are not exactly degenerate, but rather are linear combinations of the two $m = \pm 6$ states of the Ising model.

To understand the behavior in a magnetic field we add the Zeeman energy to Eq. (6) and consider the Hamiltonian

$$\begin{aligned} H_{CFZ} &= H_{CF} - g\mu_B h J_z \\ &= c_0\left(J(J+1) - 3J_z^2\right) + i\,c_1\left(J_+^2 - J_-^2\right) - g\mu_B \vec{B}.\vec{J}, \end{aligned} \tag{8}$$

where $c_1 = c_0\frac{\alpha}{4}$ and $g = \frac{7}{6}$ from the Lande rule. We plot the eigenvalues of H versus $g\mu_B h$ at two values of c_0, c_1 in Fig. 7. Constraints on the value of c_0 follow from the experimental observation in Ref. [1] that TmB_4 displays a moment of $\sim 6\,\mu_B$ for a field along the z (i.e., c) axis. In the x direction

the full moment $\sim 6\ \mu_B$ is regained only for a field $B \gtrsim 6$ T. At $c_0 \sim .01$ meV the condition on the magnetic moments is satisfied, while smaller (larger) values of c_0 make the recovery in the transverse direction occur at lower (higher) values of the B field. The choice of c_1 is less stringently constrained, from the estimates on α we expect $c_1 \lesssim .02$ meV. The value of $c_0 \sim .01$ meV is too small to create a gap near $B \sim 0$ between the two levels that cross there, and hence we see that the moment of Tm can be modeled well by an effective Ising model. The small but nonzero value of c_1 plays the role of mixing the $m = 6$ components with lower $m = 4,2,0\ldots$ as discussed below; this feature is essential for the emergence of a Kondo-Ising model.

VI. KONDO ISING MODEL FOR TmB_4

We next formulate a minimal model for describing TmB_4 following the method indicated in Refs. [39,40] and Ref. [41] in the context of the mixed valent compound $TmSe_2$. We first set up a local type Anderson or Hirst type model that incorporates the crystal field split Tm levels and the boron bands that hybridize with these. The Tm ion is considered to be in its ground (excited) state with 12 (13) electrons. The relevant $4f^{12}$ level has eigenstates given by $|J_0 M_0\rangle$ with $J_0 = 6$ and $-6 \leqslant M_0 \leqslant 6$. The excited state $4f^{13}$ has eigenstates given by $|J_1 M_1\rangle$ with $J_1 = \frac{7}{2}$ and $-\frac{7}{2} \leqslant M_1 \leqslant \frac{7}{2}$. We will use these ranges for the symbols M_0, M_1, and their primed versions below. The ground state of the ionic Hamiltonian was discussed in Sec. V. We use a similar scheme for the first excited state with angular momentum J_1 and write a generalized ionic Hamiltonian:

$$\begin{aligned} H_{\rm ion} = &\sum_{M_0} E_{12}(M_0)|J_0 M_0\rangle\langle J_0 M_0| \\ &+ \sum_{M_1} E_{13}(M_1)|J_1 M_1\rangle\langle J_1 M_1| \\ &+ ic_1\{\,|J_0 M_0+2\rangle\langle J_0 M_0| - \text{H.c.}\} \\ &+ ic_1'\{\,|J_1 M_1+2\rangle\langle J_1 M_1| - \text{H.c.}\}, \end{aligned} \tag{9}$$

and

$$E_{12} = c_0\big(J_0(J_0+1) - 3M_0^2\big) \tag{10}$$

$$E_{13} = c_0'\big(J_1(J_1+1) - 3M_1^2\big). \tag{11}$$

In this formulation, c_1 plays the role of quantum corrections to the otherwise diagonal model, which contains a preference for the largest magnitude $M_0 = \pm 6$. As discussed in Sec. V, the role of c_1 is to mix states $M_0 = \pm 4, \pm 2\ldots$ into these states and to slightly lift the degeneracy between $M_0 = \pm 6$. Clearly terms with c_1' play a similar role in the higher multiplet. We could ignore c_1 and proceed with the pure Ising model, but we will see below that these mixing terms play an important role in producing the Kondo-Ising model. Our full Hamiltonian $H_{\rm total}$ has two terms in addition to $H_{\rm ion}$. First we have the band energy

$$H_{\rm band} = \sum_{kjm} \varepsilon_{kjm} C_{jm}^\dagger(k) C_{jm}(k), \tag{12}$$

where we have projected the conduction electron states into angular momentum resolved states about the Tm atom assumed to be at the center, i.e., $C_\sigma^\dagger(\vec{k}) = \sum_{jm}\langle \vec{k}\sigma|kjm\rangle C_{jm}^\dagger(k)$. Second we have a mixing term between the conduction and the f electrons. To write this we temporarily forget about the CF terms—thus assuming that angular momentum is conserved, we write:

$$H_{\rm mix} = \sum_{j=\frac{5}{2}}^{\frac{7}{2}} \sum_{m_j=-j}^{j} \sum_k V_k^{(j)}(f_{jm}^\dagger C_{jm}(k) + \text{H.c.}), \tag{13}$$

where $V_k^{(j)}$ is a hybridization matrix element. We have denoted the angular momentum resolved f-level fermion as f_{jm}, here the allowed values $j = \frac{5}{2}, \frac{7}{2}$, are found by adding $L = 3$ from the f level and the spin half of the electron. Since the f^{13} and f^{12} states are analogous to bound complexes of electrons, it is convenient to rewrite Eq. (13) as

$$\begin{aligned} H_{\rm mix} = &\sum_{k,j,m_j} \sum_{M_0,M_1} V_k^{(j)}\langle J_0 M_0 j m_j|J_1 M_1\rangle \\ &\times (C_{jm_j}^\dagger(k)\,|J_0 M_0\rangle\langle J_1 M_1| + \text{H.c.}), \end{aligned} \tag{14}$$

where the Clebsch-Gordon coefficient $\langle J_0 M_0 j m_j|J_1 M_1\rangle$ enforces $M_0 + m_j = M_1$. The allowed ranges of the variables M_0, M_1, j, m_j are summarized as $|M_0| \leqslant 6$, $|M_1| \leqslant \frac{7}{2}$, $j = \frac{7}{2}$ or $j = \frac{5}{2}$, and $|m_j| \leqslant j$. We should view $|J_0 M_0\rangle$ as a bound complex of the 12-f electrons and similarly the state $|J_1 M_1\rangle$. The transition between these by adding an f electron is expected to have a small matrix element, which is absorbed in to the symbol $V_k^{(j)}$. The total Hamiltonian is thus

$$H_{\rm total} = H_{\rm ion} + H_{\rm band} + H_{\rm mix}. \tag{15}$$

We can find the analog of the Kondo model from Eq. (15) by using the standard Coqblin-Schrieffer transformation [42]. We may symbolically write it as $H_{eff} = H_{\rm mix}.\frac{1}{\Delta}.H_{\rm mix}$, where the intermediate state energy $\Delta \sim E_{13} - E_{12}$. We thus write down the effective low energy model the Kondo-Ising model for $|J| = 6$ as:

$$\begin{aligned} H_{KI} = &-\sum J_K(C_{k'j'm_j'}^\dagger C_{kjm_j})|J_0 M_0'\rangle\langle J_0 M_0| \\ &\times \delta_{m_j+M_0,M_1}\delta_{m_j'+M_0',M_1} + H_{CFZ}, \\ H_{CFZ} = &-3c_0\sum_{M_0} M_0^2|J_0 M_0\rangle\langle J_0 M_0| \\ &+ ic_1\sum_{M_0}(\,|J_0 M_0+2\rangle\langle J_0 M_0| - \text{H.c.}) - g\mu_B\vec{B}.\vec{J}, \end{aligned} \tag{16}$$

where we added the CFZ term from Eq. (8) after discarding a constant. We expect $c_0 \sim .01$ meV and $c_1 \sim .02$ meV. Given the allowed range of the variables, we see that the permissible transitions are governed by $M_0' - M_0 = m_j - m_j'$. Its maximum magnitude is 7 from the range on the right hand side $|m_j|, |m_j'| \leqslant \frac{7}{2}$. Hence the states $M_0 = 6$ and $M_0 = -6$ cannot be connected by Eq. (16) directly. Therefore the model cannot be immediately mapped into a simple effective Kondo-Ising model, where all transitions between allowed M_0's are possible. However we recall that the mixing term (i.e.,

c_1 etc.) in H_{CFZ} allows a mixing between $|M_0| = 6$ and lower values in steps of 2. This model can be further mapped into the Ising doublet manifold by using higher order degenerate perturbation theory in H_{KI} and c_1. In summary it requires a careful consideration of the various mixing terms to recover the Kondo-Ising model with a full range of angular momentum.

Within a perturbative approach in c_1 (i.e., α) it is clear that an effective Kondo Ising model emerges with the full range of allowed transitions. We also see from a standard argument (see Ref. [41]) that the elimination of the conduction electrons in Eq. (16) leads to a long ranged RKKY interaction of the Ising type. Such a model is of much interest theoretically [43–45] and could also be invoked at the lowest order to understand the experiments on the magnetization plateaux in this system [7]. We should note that quantum effects, coming in at higher orders in α (i.e., c_1) might be relevant in obtaining a good understanding of the anisotropic magnetic response.

VII. CONCLUSION

In this paper we examine the electronic and magnetic characteristics of TmB_4. Our results from an *ab initio* density functional theory approach provide insight into simplifications of the lattice in reduced tight-binding models. In the a-b plane, $4f$-$2p_z$ hybridization around the M point is a strong contributor to the in-plane conductivity. We have also found effective 1-D conduction along the c axis, indicated by relatively flat segments of the Fermi surface which can be found along the Γ-Z path. For the largest of these surfaces, we have calculated the effective mass ratio to be $\|m_{zz}/m_{xx}\| = 0.08$. We then examined the local structure, building a simplified crystal field model containing the essential physics and which led to a description of the pseudo-Ising nature of the ground state, in which the degeneracy has been slightly lifted by off-diagonal terms originating from the lack of inversion symmetry at the Tm site.

From this point of departure, we constructed a Hamiltonian consisting of a band term, an ionic term, and a mixing term. Using the Coqblin-Schrieffer transformation, we constructed an effective low-energy model, an effective Kondo-Ising type model, in which the (quantum) off-diagonal terms in the crystal field Hamiltonian are necessary in recovering the full range of angular momentum. At low magnetic fields $|B| \lesssim 10$ T the Ising approximation of the Kondo model is validated for our choice of the anisotropy constant c_0. Further experimental studies in transverse fields should help to refine the values of constants c_0 and c_1 in Eq. (16). It seems plausible that the elimination of the conduction electrons would lead to an RKKY-type Ising model with some quantum corrections and thus refine the usual starting point of studies on the magnetization plateaux [44]. Using the experimental distance and moment, we estimate that the long ranged dipolar exchange J is ~ 0.74 K at the nearest neighbor separation, and hence this needs to be added to the RKKY type interaction for obtaining the magnetic behavior at low T.

ACKNOWLEDGMENTS

The work at UCSC was supported by the U.S. Department of Energy (DOE), Office of Science, Basic Energy Sciences (BES) under Award No. DE-FG02-06ER46319. This work also used the Extreme Science and Engineering Discovery Environment (XSEDE), which is supported by National Science Foundation Grant No. ACI-1053575. We thank Alex Hewson, Sreemanta Mitra, Christos Panagopoulos, Art Ramirez, and Pinaki Sengupta for helpful discussions on the project. We would also like to thank José J. Baldoví, Alejandro Gaita Ariño, Chris Greene, Levi Hall, Jennifer Keller, Klaus Koepernick, and Erik Ylvisaker for fruitful discussions.

[1] K. Siemensmeyer, E. Wulf, H.-J. Mikeska, K. Flachbart, S. Gabáni, S. Mat'aš, P. Priputen, A. Efdokimova, and N. Shitsevalova, Phys. Rev. Lett. **101**, 177201 (2008).
[2] S. S. Sunku, T. Kong, T. Ito, P. C. Canfield, B. S. Shastry, P. Sengupta, and C. Panagopoulos, Phys. Rev. B **93**, 174408 (2016).
[3] H. Kageyama, K. Yoshimura, R. Stern, N. V. Mushnikov, K. Onizuka, M. Kato, K. Kosuge, C. P. Slichter, T. Goto, and Y. Ueda, Phys. Rev. Lett. **82**, 3168 (1999).
[4] B. S. Shastry and B. Sutherland, Physica B+C **108**, 1069 (1981).
[5] Z. P. Yin and W. E. Pickett, Phys. Rev. B **77**, 035135 (2008).
[6] W. N. Lipscomb and D. Britton, J. Chem. Phys. **33**, 275 (1960).
[7] S. Mat'aš, K. Siemensmeyer, E. Wheeler, E. Wulf, R. Beyer, T. Hermannsdörfer, O. Ignatchik, M. Uhlarz, K. Flachbart, S. Gabáni *et al.*, J. Phys.: Conf. Ser. **200**, 032041 (2010).
[8] K. Wierschem, S. S. Sunku, T. Kong, T. Ito, P. C. Canfield, C. Panagopoulos, and P. Sengupta, Phys. Rev. B **92**, 214433 (2015).
[9] L. Ye, T. Suzuki, and J. Checkelsky, Phys. Rev. B **95**, 174405 (2017).
[10] T. Mori, T. Takimoto, A. Leithe-Jasper, R. Cardoso-Gil, W. Schnelle, G. Auffermann, H. Rosner, and Y. Grin, Phys. Rev. B **79**, 104418 (2009).
[11] S. Okada, K. Kudou, Y. Yu, and T. Lundström, Jpn. J. Appl. Phys. **33**, 2663 (1994).
[12] P. Hohenberg and W. Kohn, Phys. Rev. **136**, B864 (1964).
[13] J. Towns, T. Cockerill, M. Dahan, I. Foster, K. Gaither, A. Grimshaw, V. Hazlewood, S. Lathrop, D. Lifka, G. D. Peterson *et al.*, Comput. Sci. Eng. **16**, 62 (2014).
[14] K. Koepernik and H. Eschrig, Phys. Rev. B **59**, 1743 (1999).
[15] J. P. Perdew, K. Burke, and M. Ernzerhof, Phys. Rev. Lett. **77**, 3865 (1996).
[16] M. T. Czyżyk and G. A. Sawatzky, Phys. Rev. B **49**, 14211 (1994).
[17] E. R. Ylvisaker, W. E. Pickett, and K. Koepernik, Phys. Rev. B **79**, 035103 (2009).
[18] H. Eschrig, K. Koepernik, and I. Chaplygin, J. Solid State Chem. **176**, 482 (2003).
[19] A. H. Nevidomskyy and P. Coleman, Phys. Rev. Lett. **102**, 077202 (2009).
[20] L. L. Lev, J. Krempaský, U. Staub, V. A. Rogalev, T. Schmitt, M. Shi, P. Blaha, A. S. Mishchenko, A. A. Veligzhanin, Y. V. Zubavichus *et al.*, Phys. Rev. Lett. **114**, 237601 (2015).
[21] F. Tran, F. Karsai, and P. Blaha, Phys. Rev. B **89**, 155106 (2014).

[22] J. P. Allen and G. W. Watson, Phys. Chem. Chem. Phys. **16**, 21016 (2014).

[23] M. S. Dresselhaus, G. Dresselhaus, and A. Jorio, *Group Theory: Application to the Physics of Condensed Matter* (Springer Science & Business Media, Berlin, Heidelberg, Germany, 2007).

[24] T. Tanaka and Y. Ishizawa, J. Phys. C: Solid State Phys. **18**, 4933 (1985).

[25] J. H. Forsberg, Y. Marcus, T. Moeller, U. Krüerke, and E. Schleitzer-Rust, *Gmelin Handbook of Inorganic Chemistry. Sc, Y, La-Lu-Rare Earth Elements. Pt. D 6. Ion Exchange and Solvent Extraction Reactions, Organometallic Compounds: System-number 39* (Springer, Berlin, Heidelberg, Germany, 1983).

[26] M. Dirken and L. de Jongh, Solid State Commun. **64**, 1201 (1987).

[27] A. P. Ramirez, L. F. Schneemeyer, and J. V. Waszczak, Phys. Rev. B **36**, 7145 (1987).

[28] L. Onsager, Phys. Rev. **65**, 117 (1944).

[29] K. Stevens, Proc. Phys. Soc. London, Sect. A **65**, 209 (1952).

[30] G. Williams and L. L. Hirst, Phys. Rev. **185**, 407 (1969).

[31] J. Mulak and Z. Gajek, *The Effective Crystal Field Potential* (Elsevier, Kidlington, UK, 2000).

[32] In vacuum the electron affinities of boron, oxygen, and fluorine are respectively 26.7, 141, and 328 (in kJ/mol), as per http://periodictable.com/Properties/A/ElectronAffinity.v.log.html. These vary widely in solids, but boron is known to flip sign and have negative electron affinity in several materials of interest, including hexagonal boron nitride BN; see K. P. Loh, I. Sakaguchi, M. N. Gamo, S. Tagawa, T. Sugino, and T. Ando, App. Phys. Lett. **74**, 28 (1999).

[33] $a_1 = \{1.318350, 2.206650, 0.845880\}; a_2 = \{1.318350, 2.206650, -0.845880\}; a_3 = \{-2.206650, -1.318350, -0.845880\}; a_4 = \{-2.206650, -1.318350, 0.845880\}$.

[34] $d_1^1 = \{1.931700, -0.705000, -1.995000\}; d_1^2 = \{1.931700, -0.705000, 1.995000\}; d_1^3 = \{0.705000, -1.931700, -1.995000\} d_1^4 = \{0.705000, -1.931700, 1.995000\}; d_2^1 = \{-1.593300, 1.593300, -1.995000\}; d_2^2 = \{-1.593300, 1.593300, 1.995000\}$.

[35] $s_1 = \{0.119850, 1.910550, -1.995000\}; s_2 = \{0.119850, 1.910550, 1.995000\}; s_3 = \{1.614450, 1.008150, -1.995000\}; s_4 = \{1.614450, 1.008150, 1.995000\}; s_5 = \{-1.008150, -1.614450, -1.995000\}; s_6 = \{-1.008150, -1.614450, 1.995000\}; s_7 = \{-1.910550, -0.119850, -1.995000\}; s_8 = \{-1.910550, -0.119850, 1.995000\}$.

[36] K.-G. Lee, B.-Y. Yu, C.-H. Pyun, and S.-I. Mho, Solid State Commun. **122**, 485 (2002).

[37] N. Chang, J. B. Gruber, R. P. Leavitt, and C. A. Morrison, J. Chem. Phys. **76**, 3877 (1982).

[38] N. Jeevanjee, *An Introduction to Tensors and Group Theory for Physicists* (Springer, Cham, Switzerland, 2011).

[39] M. Baliña and A. Aligia, Solid State Commun. **75**, 65 (1990).

[40] H. Lustfeld, Physica B+C **113**, 69 (1982).

[41] A. C. Hewson, *The Kondo Problem to Heavy Fermions*, Vol. 2 (Cambridge University Press, Cambridge, UK, 1997), see Eqs. (9.25, 9.26).

[42] B. Coqblin and J. Schrieffer, Phys. Rev. **185**, 847 (1969).

[43] Y. I. Dublenych, Phys. Rev. Lett. **109**, 167202 (2012).

[44] M. Shahzad and P. Sengupta, arXiv:1701.04979.

[45] W. C. Huang, L. Huo, J. J. Feng, Z. B. Yan, X. T. Jia, X. S. Gao, M. H. Qin, and J.-M. Liu, EPL (Europhysics Letters) **102**, 37005 (2013).